10 QMC for Nonequilibrium Systems

Philipp Werner
Department of Physics
University of Fribourg

Contents

E. Pavarini, E. Koch, A. Lichtenstein, and D. Vollhardt (eds.)
Understanding Correlated Materials with DMFT
Modeling and Simulation Vol. 15
Forschungszentrum Jülich, 2025, ISBN 978-3-95806-813-1
http://www.cond-mat.de/events/correl25

1 Introduction

Quantum impurity models play an important role in nanoscience as representations of quantum dots, and in condensed matter physics as auxiliary systems, whose self-consistent solution provides the dynamical mean field theory (DMFT) [1] description of lattice models. A quantum impurity model describes a system with a finite-dimensional Hilbert space ("dot"), which is coupled to one or several infinite but noninteracting systems ("baths"). The equilibrium properties of quantum impurity models are by now reasonably well understood theoretically, and in many cases the properties of interest can be computed numerically to high accuracy.

The nonequilibrium properties of quantum impurity models are much less understood, but they are relevant in connection with transport studies on quantum dots [2] and the DMFT description of pump-probe experiments on solids [3]. Different protocols can be considered to drive a quantum impurity model out of equilibrium. If a system is coupled to more than one reservoir, a chemical potential or temperature difference between the reservoirs can generate a nonequilibrium steady state in which current flows from one reservoir to another across the dot. One can also consider the relaxation to a steady state from an atypical initial condition ("quench"). In the DMFT context, the nonequilibrium reservoirs are selfconsistently computed and represent the lattice environment during the transient evolution of a perturbed system [4], or in a nonequilibrium steady-state situation [5]. While the basic formalism for dealing with these problems was established by Schwinger [6] and Keldysh [7] in the early 1960s, the calculation of unbiased results for generic nonequilibrium situations remains a challenge.

Several numerical techniques have been applied to time-dependent problems in interacting quantum dots. Numerical renormalization group methods [8] provide accurate results for the relaxation dynamics in dots with equilibrium baths. Path integral sampling techniques introduced in the quantum chemistry context [9] have been extended to the quantum dot problem [10] and recent powerful implementations make use of a tensor-train representation of the influence functional of the bath [11, 12]. The time-dependent non-crossing approximation [13] and its higher-order generalizations [14] allows an efficient treatment of the strong-correlation regime, but the correct description of Kondo resonances or weakly correlated states remains a challenge. The time-dependent density matrix renormalization group has also been used to study the transport properties of quantum dots coupled to one-dimensional reservoirs [15, 16].

In this chapter, we discuss quantum Monte Carlo (QMC) methods based on the unbiased sampling of diagrammatic expansions [17]. For equilibrium properties, these so-called continuous-time QMC methods enabled numerically efficient studies of a wide range of impurity problems, and their adaptation to the real-time contour yields potentially useful solvers for quantum dot studies and nonequilibrium DMFT. We provide a systematic analysis of the real-time diagrammatic approach, including a discussion of the strengths and weaknesses of these methods, and the regimes in which accurate results can be obtained. We also briefly discuss alternative schemes which avoid the sampling of disconnected diagrams, as well as recent developments which replace the Monte Carlo sampling of diagrams by an efficient explicit calculation of the integrals over diagram weights. The QMC part is taken from Refs. [18] and [19].

2 General formalism and model

2.1 Weak- and strong-coupling approach

A quantum impurity model is described by a Hamiltonian of the form

$$H_{QI} = H_{\text{dot}} + H_{\text{bath}} + H_{\text{mix}}. \tag{1}$$

Here H_{dot} describes a system with a finite-dimensional Hilbert space, which we refer to as the "impurity", or "dot", H_{bath} describes one or more infinite reservoirs characterized by a continuum of levels, and H_{mix} the coupling between the impurity and the reservoirs. We assume that at time $t = 0$ the state of the system is described by the density matrix ρ_0.

The theoretical task is to evaluate the expectation value $\langle \mathcal{O}(t) \rangle$ of an operator $\mathcal{O}$ at time t, i.e. to compute

$$\langle \mathcal{O}(t) \rangle = \text{Tr}\left[\rho_0 \, e^{i\int_0^t dt' H_{QI}(t')} \mathcal{O} \, e^{-i\int_0^t dt'' H_{QI}(t'')} \right] \tag{2}$$

(the generalization to operators with multiple time dependences is straightforward and will not be written explicitly). A nonequilibrium situation can arise through a time dependence of the parameters in H_{QI} ("irradiation"), through the correlators of the operators in H_{bath} ("nonequilibrium reservoirs") or through an initial density matrix ρ_0 which is different from the long-time limit ("quench").

One can view the expectation value in Eq. (2) as an evolution on the Schwinger-Keldysh contour illustrated in Fig. 1 from time $t = 0$ (when the system is described by the density matrix ρ_0) to time t (at which the operator is measured), and then back to time 0 [6]. Our general strategy for evaluating Eq. (2) is to write H_{QI} as a sum of two terms: one, H_0 for which the time evolution can be treated exactly and another, H_I, which is treated by a perturbative expansion. The expansion in H_I generates a series of diagrams, which are sampled stochastically, using an importance sampling which accepts or rejects proposed diagrams on the basis of their contributions to $\langle \tilde{\mathcal{O}} \rangle$ (in the discussed implementations we use $\tilde{\mathcal{O}} = 1$).

Two types of expansion are considered: One is a "weak coupling" method, in which H_{dot} is partitioned into a quadratic part H^0_{dot} and an interacting part H_U, the combination $H^0_{\text{dot}} + H_{\text{mix}} + H_{\text{bath}}$ is treated exactly, ρ_0 is taken to be the corresponding density matrix, and the expansion is constructed in terms of H_U. The other is a "strong coupling" (more properly, "hybridization") expansion in which H_{dot} and H_{bath} are treated exactly, ρ_0 is the density matrix corresponding

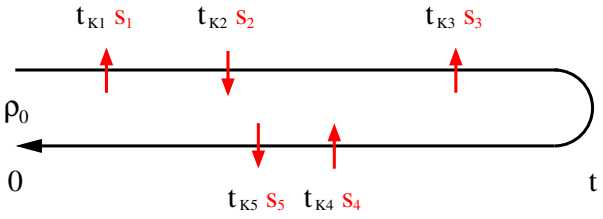

Fig. 1: *Illustration of the Schwinger-Keldysh contour and example of a Monte Carlo configuration corresponding to perturbation order $n = 5$ and $n_+ = 3$, $n_- = 2$. (From Ref. [18])*

to the direct product of a lead density matrix and a density matrix describing the dot decoupled from the leads, and $H_{\rm mix}$ is treated as a perturbation. The hybridization expansion for nonequilibrium problems was originally introduced by Mühlbacher and Rabani [20] in the context of noninteracting electrons coupled to phonons, and has been applied to interacting dots in Ref. [21]. An essentially identical formalism has also been discussed in Ref. [22]. The real-time version of the weak-coupling approach was introduced in Ref. [18].
Methods based on stochastically sampled diagrammatic expansions [23–26] have had considerable success in treating equilibrium quantum impurity problems at temperature $T > 0$ and they have become the main workhorse for DMFT [17]. In equilibrium calculations, the expansion can be formulated on the imaginary time axis $0 \le \tau < 1/T$ (only one contour is needed) and the expansion parameter is $-H_I(\tau) = e^{\tau H_0}(-H_I)\, e^{-\tau H_0}$. The fermionic sign problem can be avoided in many relevant situations, so that average perturbation orders of $\mathcal{O}(100)$ can be easily treated. Three related sources of difficulty arise in nonequilibrium setups. First, the expansion must be done for real times, so the time evolution introduces complex phases and the diagrams come with factors of i to powers relating to the perturbation order. Second, two contour branches rather than one are required (Fig. 1), doubling the perturbation order required to reach a given time. Third, in nonequilibrium situations it may be essential to build up the correct entanglement between the impurity and the bath before observables can be measured. All of these factors limit the range over which accurate results can be obtained, but the crucial constraint is the dynamical sign problem resulting from the oscillatory convergence.

2.2 Model

In the following discussions, we consider a dot consisting of a single spin-degenerate level with a Hubbard interaction U, coupled by hybridization V to two reservoirs ("leads") labeled by $\alpha = L, R$, which can have different chemical potentials μ_α.
The different terms of the Hamiltonian are

$$H_{\rm bath} = \sum_{\alpha=L,R} \sum_{p,\sigma} \big(\varepsilon^\alpha_{p,\sigma} - \mu_\alpha\big) a^{\alpha\dagger}_{p,\sigma} a^\alpha_{p,\sigma}, \tag{3}$$

$$H_{\rm mix} = \sum_{\alpha=L,R} \sum_{p,\sigma} \big(V^\alpha_p a^{\alpha\dagger}_{p,\sigma} d_\sigma + \text{h.c.}\big), \tag{4}$$

$$H^0_{\rm dot} = \big(\varepsilon_d + U/2\big) \sum_\sigma n_{d,\sigma}, \tag{5}$$

$$H_U = U\big(n_{d,\uparrow} n_{d,\downarrow} - (n_{d,\uparrow} + n_{d,\downarrow})/2\big). \tag{6}$$

Here, d_σ ($a^\alpha_{p,\sigma}$) annihilates the spin-σ electron on the dot (spin-σ and lead-α bath electron with index p), $n_{d,\sigma} = d^\dagger_\sigma d_\sigma$ is the spin-density on the dot, and ε_d ($\varepsilon^\alpha_{p,\sigma}$) denotes the dot (bath level) energy. For convenience, we also define

$$H_{\rm dot} = H^0_{\rm dot} + H_U. \tag{7}$$

The initial density matrix is such that the correlators of lead operators are

$$\big\langle a^{\alpha\dagger}_{p,\sigma} a^\beta_{p',\sigma'} \big\rangle = \delta_{\alpha,\beta} \delta_{p,p'} \delta_{\sigma,\sigma'} f_{T_\alpha}(\varepsilon^\alpha_{p,\sigma} - \mu_\alpha), \tag{8}$$

where $f_T(x) = 1/(e^{x/T}+1)$ is the Fermi distribution function for temperature T. The statement that H_{bath} describes infinite reservoirs implies that Eq. (8) holds at all times.
The model has three important energy scales: ε_d which controls the steady state dot occupancy, the interaction scale U, and the level broadening

$$\Gamma^\alpha(\omega) = \pi \sum_p \left|V_p^\alpha\right|^2 \delta(\omega - \varepsilon_p^\alpha) \tag{9}$$

associated with lead α. The total level broadening is

$$\Gamma = \Gamma^L + \Gamma^R \tag{10}$$

and the dimensionless measure of interaction strength is U/Γ. Very roughly, strong coupling physics appears for $U \gtrsim \pi\Gamma$ while the opposite limit is reasonably well described by perturbation theory in U.

3 Weak-coupling algorithm

3.1 Auxiliary-field formalism

In the weak coupling expansion we treat $H_0 \equiv H_{\text{dot}}^0 + H_{\text{mix}} + H_{\text{bath}}$ exactly and H_U as a perturbation. H_0 is a noninteracting problem for which the density matrix and all correlators of the dot-lead system can be determined exactly. We take the initial density matrix to be the steady-state density matrix corresponding to H_0,

$$\rho_0 = \frac{e^{-\beta H_0}}{\operatorname{Tr} e^{-\beta H_0}}, \tag{11}$$

and we turn on the interaction at time $t = 0_+$. Here we assume that the temperatures of the two leads are identical; the generalization to unequal temperatures is straightforward.
We formulate the perturbation theory in U as a real-time adaptation of the continuous-time auxiliary field method of Ref. [26], but the real-time version of the weak-coupling approach by Rubtsov *et al.* [23] works analogously. Considering $\tilde{\mathcal{O}} = 1$, the starting point for the real-time auxiliary field method is the following expression for the identity

$$1 = \operatorname{Tr} \rho_0 \, e^{it(H_0+H_U-K/t)} \, e^{-it(H_0+H_U-K/t)}, \tag{12}$$

with K a constant which is in principle arbitrary and may be chosen to optimize the simulation. Using an interaction representation in which the time evolution of the operators is given by $O(s) = e^{isH_0} \, O \, e^{-isH_0}$ we can rewrite Eq. (12) as

$$1 = \operatorname{Tr} \rho_0 \Big(\tilde{\mathcal{T}} e^{i\int_0^t ds(H_U(s)-K/t)}\Big) \, e^{itH_0} \, e^{-itH_0} \Big(\mathcal{T} e^{-i\int_0^t ds(H_U(s)-K/t)}\Big), \tag{13}$$

with $\mathcal{T}$ the time ordering and $\tilde{\mathcal{T}}$ the anti-time ordering operator, and expand the time-ordered exponentials into a power series. This leads to the expression

$$1=\mathrm{Tr}\,\rho_0\sum_m(-iK/t)^m\int_0^t d\tilde{t}_1\cdots\int_{\tilde{t}_{m-1}}^t d\tilde{t}_m e^{i\tilde{t}_1H_0}(1-tH_U/K)\cdots e^{i(\tilde{t}_m-\tilde{t}_{m-1})H_0}(1-tH_U/K)e^{i(t-\tilde{t}_m)H_0}$$
$$\times\sum_n(iK/t)^n\int_0^t dt_1\cdots\int_{t_{n-1}}^t dt_n e^{-i(t-t_n)H_0}(1-tH_U/K)\cdots e^{-i(t_2-t_1)H_0}(1-tH_U/K)e^{-it_1H_0}. \tag{14}$$

Using the explicit form for H_U (Eq. (6)) and the auxiliary field decomposition of Ref. [27] we can rewrite the interaction term as

$$1-(tU/K)\big(n_{d,\uparrow}n_{d,\downarrow}-(n_{d,\uparrow}+n_{d,\downarrow})/2\big)=1/2\sum_{s=-1,1}e^{\gamma s(n_{d,\uparrow}-n_{d,\downarrow})}, \tag{15}$$

$$\cosh(\gamma)=1+(tU)/(2K). \tag{16}$$

Note that the constant K has been introduced to enable this decomposition. The trace is now a product of exponentials of one-body operators,

$$1=\sum_m\sum_n(-i)^m i^n(K/2t)^{m+n}\sum_{\tilde{s}_1,\ldots,\tilde{s}_n}\sum_{s_1,\ldots,s_m}\int_0^t d\tilde{t}_1\cdots\int_{\tilde{t}_{m-1}}^t d\tilde{t}_m\int_0^t dt_1\cdots\int_{t_{n-1}}^t dt_n\prod_\sigma\frac{1}{\mathrm{Tr}\,e^{-\beta H_{0,\sigma}}}\mathrm{Tr}\,e^{-\beta H_{0,\sigma}}\times$$
$$e^{i\tilde{t}_1H_{0,\sigma}}e^{\gamma\tilde{s}_1\sigma n_{d,\sigma}}\cdots e^{i(\tilde{t}_m-\tilde{t}_{m-1})H_{0,\sigma}}e^{\gamma\tilde{s}_m\sigma n_{d,\sigma}}e^{-i(\tilde{t}_m-t_n)H_{0,\sigma}}e^{\gamma s_n\sigma n_{d,\sigma}}\cdots e^{-i(t_2-t_1)H_{0,\sigma}}e^{\gamma s_1\sigma n_{d,\sigma}}e^{-it_1H_{0,\sigma}}$$

and can be expressed [26] in terms of determinants of two $(n+m)\times(n+m)$ matrices

$$N_\sigma^{-1}=e^{S_\sigma}-iG_{0,\sigma}\big(e^{S_\sigma}-I\big) \tag{17}$$

as

$$1=\sum_m\sum_n(-i)^m i^n(K/2t)^{m+n}\sum_{\tilde{s}_1,\ldots,\tilde{s}_n}\sum_{s_1,\ldots,s_m}\int_0^t d\tilde{t}_1\cdots\int_{\tilde{t}_{m-1}}^t d\tilde{t}_m\int_0^t dt_1\cdots\int_{t_{n-1}}^t dt_n\prod_\sigma\det N_\sigma^{-1}. \tag{18}$$

Here, $e^{S_\sigma}=\mathrm{diag}(e^{\gamma\tilde{s}_1\sigma},\ldots,e^{\gamma\tilde{s}_m\sigma},e^{\gamma s_n\sigma},\ldots,e^{\gamma s_1\sigma})$ and $G_{0,\sigma}$ is given by

$$G_{0,\sigma}(t'_K,t''_K)=\begin{cases}G^<_{0,\sigma}(t',t''), & t'_K<t''_K\\ G^>_{0,\sigma}(t',t''), & t'_K\geq t''_K\end{cases}. \tag{19}$$

In the above expression, $G_0^<(t,t')=i\langle d^\dagger(t')d(t)\rangle_0$, $G_0^>(t,t')=-i\langle d(t)d^\dagger(t')\rangle_0$, t_K is the "Keldysh time" coordinate along the unfolded Keldysh contour (Fig. 1) and t the physical time corresponding to t_K. In quantum dot systems, these Green functions can usually be calculated analytically [28], while in nonequilibrium DMFT simulations, they are the output of the self-consistency procedure [4]. In our quantum dot applications, we will use the infinite bandwidth limit in which the level broadening is independent of ω, so that

$$G_0^{</>}(t',t'')=\pm i\sum_{\alpha=L,R}\Gamma^\alpha\int\frac{d\omega}{2\pi}e^{-i\omega(t'-t'')}\frac{1\mp\tanh\left(\frac{\omega-\mu_\alpha}{2T}\right)}{(\omega-\varepsilon_d-U/2)^2+\Gamma^2}, \tag{20}$$

with the upper sign pertaining to $G_0^<$ and the lower sign to $G_0^>$.

3.2 Detailed balance and fast updates

The algorithm samples auxiliary Ising spin configurations $\{(t_{K,1}, s_1), (t_{K,2}, s_2), \ldots (t_{K,n}, s_n)\}$ time ordered along the Keldysh contour $0 \to t \to 0$ (see Fig. 1) by random insertions and removals of spins. The complex "weight" of a spin configuration is given by

$$w(\{(t_{K,1}, s_1), (t_{K,2}, s_2), \ldots (t_{K,n}, s_n)\}) = (-i^{n_-})(i^{n_+})(Kdt/2t)^{n_-+n_+} \prod_\sigma \det N_\sigma^{-1}, \quad (21)$$

where n_+ denotes the number of spins on the forward contour and n_- the number of spins on the backward contour ($n = n_+ + n_-$).
The detailed balance condition for insertion/removal of a spin is similar to the imaginary time formulation of Ref. [26]. Assuming that we pick a random time on the unfolded contour of length $2t$ and a random direction for this new spin, $p^{\text{prop}}(n-1 \to n) = (1/2)(dt/(2t))$, and propose to remove this spin with probability $p^{\text{prop}}(n \to n-1) = 1/n$ we get

$$\frac{p(n-1 \to n)}{p(n \to n-1)} = \pm i \frac{2K}{n} \prod_\sigma \frac{\det(N_n^{-1})_\sigma}{\det(N_{n-1}^{-1})_\sigma}, \quad (22)$$

with the factor $+i$ corresponding to a spin which is inserted on the forward contour and $-i$ to a spin which is inserted on the backward contour.
For the fast updates, let us consider the most complicated case, which is the insertion of a spin. This update adds one row and one column to the $(n-1)\times(n-1)$ matrix N, resulting in the $n\times n$ matrix N' (we assume here that this new row/column is the last one, n, and drop the spin index). The determinant ratio is

$$r = \frac{\det(N'^{-1})}{\det(N^{-1})} = \left(e^S - iG_0(e^S - I)\right)_{n,n} - \sum_{i=1}^{n-1} R_i \left(e^S - iG_0(e^S - I)\right)_{i,n}, \quad (23)$$

with $R_i = \sum_{j=1}^{n-1} \left(e^S - iG_0(e^S - I)\right)_{n,j} N_{j,i}$. The calculation of this quantity requires $O(n^2)$ operations. The new matrix elements are given by

$$N'_{i,j} = N_{i,j} + \frac{1}{r} L_i R_j, \quad (24)$$

$$N'_{i,n} = -\frac{1}{r} L_i, \quad (25)$$

$$N'_{n,j} = -\frac{1}{r} R_j, \quad (26)$$

$$N'_{n,n} = \frac{1}{r}, \quad (27)$$

with $i = 1, \ldots, n-1$ and $L_i = \sum_{j=1}^{n-1} N_{i,j} \left(e^S - iG_0(e^S - I)\right)_{j,n}$.
From Eq. (27) it follows that computing the determinant ratio for removing a spin is $O(1)$. The elements of the reduced matrix are obtained as

$$N_{i,j} = N'_{i,j} - \frac{N'_{i,n} N'_{n,j}}{N'_{n,n}}. \quad (28)$$

3.3 Measurement of the Green function, density and double occupancy

To measure the Green function $G_\sigma(t'_K, t''_K)$ we have to insert an operator d_σ at time t'_K and an operator $d^\dagger_\sigma$ at time t''_K. The weights of these configurations $w(\{(t_{K,1}, s_1), \dots (t_{K,n}, s_n)\}; d_\sigma(t'_K)d^\dagger_\sigma(t''_K))$ are related to those defined in Eq. (21) by

$$\frac{w(\{(t_{K,1}, s_1), \dots (t_{K,n}, s_n)\}; d(t')d^\dagger(t''))}{w(\{(t_{K,1}, s_1), \dots (t_{K,n}, s_n)\})} = \frac{1}{\det N_\sigma^{-1}} \det \left(\begin{array}{c|c} N_\sigma^{-1}(i,j) & iG_{0,\sigma}(t_{K,i}, t''_K) \\ \hline -iG_{0,\sigma}(t'_K, t_{K,j})(e^{\gamma\sigma s_j} - 1) & iG_{0,\sigma}(t'_K, t''_K) \end{array} \right). \quad (29)$$

Hence, the Green function can be obtained as the Monte Carlo average of the quantity [26]

$$\tilde{G}_\sigma(t'_K, t''_K) = G_{0,\sigma}(t'_K, t''_K) + i \sum_{i,j=1}^{n} G_{0,\sigma}(t'_K, t_{K,i}) \big((e^{S_\sigma} - 1)N_\sigma\big)_{i,j} G_{0,\sigma}(t_{K,j}, t''_K), \quad (30)$$

which yields the measurement formulas

$$G_\sigma(t'_K, t''_K) = \big\langle \tilde{G}_\sigma(t'_K, t''_K) \big\rangle, \quad (31)$$

$$n_\sigma(t_K) = 1 - i\big\langle \tilde{G}_\sigma(t_K, t_K) \big\rangle, \quad (32)$$

$$n_\uparrow n_\downarrow(t_K) = \big\langle (1 - i\tilde{G}_\uparrow(t_K, t_K))(1 - i\tilde{G}_\downarrow(t_K, t_K)) \big\rangle. \quad (33)$$

3.4 Current measurement

The current from the dot to the left lead is

$$I_L = \sum_\sigma I_{L\sigma} = -2 \,\mathrm{Im} \sum_\sigma \sum_{p \in L} V^L_{p,\sigma} \big\langle a^{L\dagger}_{p,\sigma} d_\sigma \big\rangle. \quad (34)$$

Thus, in terms of the composite lead operator $\tilde{a}^\dagger_{L,\sigma} \equiv \sum_{p\in L} V^L_{p,\sigma} a^{L\dagger}_{p,\sigma}$, we find

$$\begin{aligned} I_{L\sigma}(t) =& -2 \,\mathrm{Im}\, \mathrm{Tr}\, \rho_0 \Big(\tilde{\mathcal{T}} e^{i\int_0^t ds (H_I(s) - K/t)} \Big) e^{itH_0}\, \tilde{a}^\dagger_{L,\sigma}\, d_\sigma\, e^{-itH_0} \Big(\mathcal{T} e^{-i\int_0^t ds (H_I(s) - K/t)} \Big) \\ =& -2 \,\mathrm{Im} \sum_m \sum_n (-i)^m i^n (K/2t)^{m+n} \sum_{\tilde{s}_1, \dots, \tilde{s}_n} \sum_{s_1, \dots, s_m} \int_0^t d\tilde{t}_1 \cdots \int_{\tilde{t}_{m-1}}^t d\tilde{t}_m \int_0^t dt_1 \cdots \int_{t_{n-1}}^t dt_n \times \\ & \frac{\det N_{\bar{\sigma}}^{-1}}{\mathrm{Tr}\, e^{-\beta H_{0,\sigma}}} \mathrm{Tr} \Big[e^{-\beta H_0} e^{i\tilde{t}_1 H_{0,\sigma}} e^{\gamma \tilde{s}_1 \sigma n_{d,\sigma}} \cdots \\ & \cdots e^{\gamma \tilde{s}_m \sigma n_{d,\sigma}} e^{i(t - \tilde{t}_m) H_{0,\sigma}}\, \tilde{a}^\dagger_{L,\sigma}\, d_\sigma\, e^{-i(t - t_n) H_{0,\sigma}} e^{\gamma \sigma s_n \sigma n_{d,\sigma}} \cdots e^{\gamma s_1 \sigma n_{d,\sigma}} e^{-it_1 H_{0,\sigma}} \Big], \end{aligned} \quad (35)$$

with $\bar{\sigma}$ the spin which is opposite to σ (this spin component has no operator $\tilde{a}$ and thus simply gives the usual factor $\det N_{\bar{\sigma}}^{-1}$). The measurement of the current is thus very similar to the measurement of the Green functions, but one factor in the Wick decomposition is now

$$A(t_K, t'_K) = \begin{cases} A^<(t,t') \equiv \big\langle \tilde{a}^{L\dagger}_\sigma(t') d_\sigma(t) \big\rangle_0, & t_K \le t'_K \\ A^>(t,t') \equiv -\big\langle d_\sigma(t) \tilde{a}^{L\dagger}_\sigma(t') \big\rangle_0, & t_K > t'_K \end{cases}. \quad (36)$$

In the infinite bandwidth limit we have [18]

$$\left.\begin{matrix} A^<(t,t') \\ A^>(t,t') \end{matrix}\right\} = -2i \int \frac{d\omega}{2\pi} e^{-i\omega(t-t')} \frac{\Gamma_L\Gamma_R\big(f(\omega-\mu_L)-f(\omega-\mu_R)\big)}{(\omega-\varepsilon_d-U/2)^2+\Gamma^2}$$
$$+ 2\Gamma_L \int \frac{d\omega}{2\pi} e^{-i\omega(t-t')} \frac{(\omega-\varepsilon_d-U/2)}{(\omega-\varepsilon_d-U/2)^2+\Gamma^2} \times \begin{cases} f(\omega-\mu_L) \\ \big(f(\omega-\mu_L)-1\big) \end{cases} . \quad (37)$$

The trace factor in Eq. (35) for an n-th order diagram corresponding to the $n\times n$ matrix N_σ^{-1} is the determinant of the $(n+1)\times(n+1)$ matrix

$$M_\sigma^{-1} = \left(\begin{array}{c|c} N_\sigma^{-1}(i,j) & A(t_{K,i},t) \\ \hline -iG_{0,\sigma}(t,t_{K,j})(e^{\gamma\sigma s_j}-1) & A(t,t) \end{array}\right). \quad (38)$$

The current can thus be expressed as follows:

$$I_L = -2\,\mathrm{Im}\sum_\sigma \sum_c w_c^{I_\sigma} = -2\,\mathrm{Im}\sum_\sigma \frac{\sum_c |w_c|(w_c^{I_\sigma}/|w_c|)}{\sum_c |w_c|\phi_c} = -2\,\mathrm{Im}\sum_\sigma \Big\langle \frac{w_c^{I_\sigma}}{|w_c|}\Big\rangle_{|w_c|} \frac{1}{\langle\phi_c\rangle_{|w_c|}}, \quad (39)$$

with ϕ_c the phase of the weight w_c (Eq. (21)) and

$$\frac{w_c^{I_\sigma}}{w_c} = \frac{\det N_{\bar\sigma}^{-1}\det M_\sigma^{-1}}{\det N_{\bar\sigma}^{-1}\det N_\sigma^{-1}} = A(t,t) + \sum_{n,m} iG_{0,\sigma}(t,t_{K,n})\big((e^{S_\sigma}-1)N_\sigma\big)_{n,m} A(t_{K,m},t). \quad (40)$$

Combining Eqs. (39) and (40), the current measurement formula becomes

$$I_L = -2\,\mathrm{Im}\sum_\sigma \Big(A(t,t) + \Big\langle \sum_{n,m} iG_{0,\sigma}(t,t_{K,n})\big((e^{S_\sigma}-1)N_\sigma\big)_{n,m} A(t_{K,m},t)\phi_c\Big\rangle_{|w_c|} \frac{1}{\langle\phi_c\rangle_{|w_c|}}\Big). \quad (41)$$

The first term in this expression is the steady-state current for the non-interacting system

$$I_0 = -2\,\mathrm{Im}\,\big(2A(t,t)\big) = 8\int \frac{d\omega}{2\pi} \frac{\Gamma_L\Gamma_R\big(f(\omega-\mu_L)-f(\omega-\mu_R)\big)}{(\omega-\varepsilon_d U/2)^2+\Gamma^2}. \quad (42)$$

3.5 Improved sampling and estimators

In the particle-hole symmetric case, the parameters K of the algorithm can be chosen such that only even perturbation orders appear in the expansion. In fact, for

$$K = -\frac{tU}{4} \quad (43)$$

the spin degree of freedom effectively disappears ($e^{\gamma s\sigma} = -1$) and the algorithm becomes the real-time version of Rubtsov's weak-coupling method [23] for the particle-hole symmetric interaction term $H_U - K/t = U(n_{d,\uparrow}-\frac{1}{2})(n_{d,\downarrow}-\frac{1}{2})$ [29]. The odd perturbation orders are continuously suppressed as K approaches $-tU/4$. In order to sample only even order diagrams, it is however necessary to implement modified updates, which insert or remove two spins at the same time.

We next discuss some tricks to improve the efficiency of the current measurement [19]. First, we rewrite the expectation value of Eq. (40) as

$$A(t,t)+\int ds_1 \int ds_2\, G_{0,\sigma}(t,s_1)\left\langle i\sum_{n,m}\delta_{\mathcal{C}}(s_1,t_{K,n})\big((e^{S_\sigma}-I)N_\sigma\big)_{n,m}\delta_{\mathcal{C}}(s_2,t_{K,m})\right\rangle A(s_2,t), \quad (44)$$

where the variables s_1 and s_2 run over the entire contour and the contour delta function is defined by $\int ds\, \delta_{\mathcal{C}}(t_K,s)f(s)=f(t_K)$. It is therefore sufficient to accumulate the quantity

$$X_\sigma(s_1,s_2)=\left\langle i\sum_{n,m}\delta_{\mathcal{C}}(s_1,t_{K,n})\big((e^{S_\sigma}-1)N_\sigma\big)_{n,m}\delta_{\mathcal{C}}(s_2,t_{K,m})\right\rangle. \quad (45)$$

Furthermore, it follows from Eq. (21) that the weight of a Monte Carlo configuration changes sign if the last spin (corresponding to the largest time argument) is shifted from the forward contour to the backward contour or vice versa. Since the absolute value of the weight does not change, these two configurations will be generated with equal probability. As a result, all the terms in Eq. (44) which do not involve the last operator on the contour will cancel. It is therefore more efficient and accurate to accumulate

$$X_\sigma(s_1,s_2)=\left\langle i\sum_{l\ \text{not last}}\big(x(s_1,\text{last};s_2,l)+x(s_1,l;s_2,\text{last})\big)\right\rangle, \quad (46)$$

with $x(s_1,n;s_2,m)\equiv\delta_{\mathcal{C}}(s_1,t_{K,n})\left((e^{\Gamma_\sigma}-1)N_\sigma\right)_{n,m}\delta_{\mathcal{C}}(s_2,t_{K,m})$.
Also, by comparing the contributions to the current of the original configuration and the one with the last operator shifted from the upper to the lower contour (or vice versa), one finds that they almost (but not completely) cancel. The error bars on the current can thus be substantially reduced by appropriate symmetrizations of $X(s_1,s_2)$.

4 Hybridization expansion algorithm

4.1 Formalism

A complementary diagrammatic Monte Carlo algorithm to the one described in Sec. 3 can be obtained by performing an expansion in powers of the dot-lead hybridizations V. This simulation approach has been introduced for equilibrium systems (imaginary-time formalism) in Refs. [24, 25] and was discussed for a nonequilibrium quantum dot with phonons (but without electron-electron interactions) in Refs. [20, 22]. It has been applied to interacting dots in Refs. [18,21]. We will present here the derivation for the impurity model defined in Eqs. (3)-(6), but the method can easily be extended to general classes of impurity models by using the matrix formulation of Ref. [25].
In the hybridization expansion approach one adopts an interaction representation with respect to the dot-lead mixing, so the time evolution of the operators is given by the local part of the Hamiltonian, $H_{\rm loc}=H_{\rm dot}+H_{\rm bath}$. Considering $\tilde{\mathcal{O}}=1$, the starting point of the derivation is the identity

$$1=\mathrm{Tr}\,\rho_0\Big(\tilde{\mathcal{T}}e^{i\int_0^t ds H_{\rm mix}(s)}\Big)\,e^{itH_{\rm loc}}\,e^{-itH_{\rm loc}}\,\Big(\mathcal{T}e^{-i\int_0^t ds H_{\rm mix}(s)}\Big). \quad (47)$$

The initial state of the system is specified by the density matrix $\rho_0 = \rho_{\text{dot}} \otimes \rho_{\text{bath}}$, with ρ_{bath} a function of inverse temperature β and the chemical potentials $\mu_{L,R}$. In the calculations presented here we assume that the dot is initially empty, $\rho_{\text{imp}} = |0\rangle\langle 0|$.
Expanding the time-ordered exponentials into a power series yields

$$1 = \operatorname{Tr} \rho_0 \sum_m i^m \int_0^t d\tilde{t}_1 \cdots \int_{\tilde{t}_{m-1}}^t d\tilde{t}_m \, H_{\text{mix}}(\tilde{t}_1) \cdots H_{\text{mix}}(\tilde{t}_m) \sum_n (-i)^n \int_0^t dt_1 \cdots \int_{t_{n-1}}^t dt_n \, H_{\text{mix}}(t_n) \cdots H_{\text{mix}}(t_1). \tag{48}$$

Because $H_{\text{mix}} = \sum_\sigma \left(H_{\text{mix}}^{d_\sigma} + H_{\text{mix}}^{d_\sigma^\dagger} \right)$ with $H_{\text{mix}}^{d_\sigma} = \sum_{\alpha=L,R} \sum_p V_p^\alpha a_{p,\sigma}^{\alpha\dagger} d_\sigma$, $H_{\text{mix}}^{d_\sigma^\dagger} = \left(H_{\text{mix}}^{d_\sigma} \right)^\dagger$ and the time evolution conserves the spin, we need for each σ separately an equal number of creation and annihilation operators on the Keldysh contour $0 \to t \to 0$:

$$1 = \sum_{m_\sigma + n_\sigma = m'_\sigma + n'_\sigma} \prod_\sigma i^{m_\sigma + m'_\sigma} (-i)^{n_\sigma + n'_\sigma} \int_0^t d\tilde{t}_1^\sigma \cdots \int_{\tilde{t}_{m_\sigma - 1}^\sigma}^t d\tilde{t}_{m_\sigma}^\sigma \int_0^t d\tilde{t}_1'^\sigma \cdots \int_{\tilde{t}_{m'_\sigma - 1}^\sigma}^t d\tilde{t}_{m'_\sigma}'^\sigma \int_0^t dt_1^\sigma \cdots \int_{t_{n_\sigma - 1}^\sigma}^t dt_{n_\sigma}^\sigma \int_0^t dt_1'^\sigma \cdots \int_{t'^\sigma_{n'_\sigma - 1}}^t dt_{n'_\sigma}'^\sigma$$

$$\operatorname{Tr} \rho_0 \tilde{\mathcal{T}} \mathcal{T} \prod_\sigma H_{\text{mix}}^{d_\sigma}(\tilde{t}_1^\sigma) H_{\text{mix}}^{d_\sigma^\dagger}(\tilde{t}_1'^\sigma) H_{\text{mix}}^{d_\sigma}(\tilde{t}_2^\sigma) H_{\text{mix}}^{d_\sigma^\dagger}(\tilde{t}_2'^\sigma) \cdot\cdot e^{iH_{\text{loc}}t} e^{-iH_{\text{loc}}t} \cdot\cdot H_{\text{mix}}^{d_\sigma}(t_2^\sigma) H_{\text{mix}}^{d_\sigma^\dagger}(t_2'^\sigma) H_{\text{mix}}^{d_\sigma}(t_1^\sigma) H_{\text{mix}}^{d_\sigma^\dagger}(t_1'^\sigma), \tag{49}$$

where $\tilde{\mathcal{T}}$ is the anti-time ordering operator for the $\tilde{t}$s and $\mathcal{T}$ the time ordering operator for the ts. At this stage we can separate the bath operators $a_{p,\sigma}^\alpha$ from the dot operators d_σ and write

$$\begin{aligned}
\operatorname{Tr} = \operatorname{Tr}_d \Big[\rho_{\text{dot}} \tilde{\mathcal{T}} \mathcal{T} \prod_\sigma d_\sigma(\tilde{t}_1^\sigma) d_\sigma^\dagger(\tilde{t}_1'^\sigma) d_\sigma(\tilde{t}_2^\sigma) d_\sigma^\dagger(\tilde{t}_2'^\sigma) \cdots e^{iH_{\text{dot}}t} e^{-iH_{\text{dot}}t} \cdots d_\sigma(t_2^\sigma) d_\sigma^\dagger(t_2'^\sigma) d_\sigma(t_1^\sigma) d_\sigma^\dagger(t_1'^\sigma) \Big] \\
\times \operatorname{Tr}_{\text{bath}} \Big[\rho_{\text{bath}} \tilde{\mathcal{T}} \mathcal{T} \prod_\sigma \sum_{\tilde{p}_1 \tilde{\alpha}_1; \ldots; \tilde{p}_{m_\sigma} \tilde{\alpha}_{m_\sigma}} \sum_{\tilde{p}'_1 \tilde{\alpha}'_1; \ldots; \tilde{p}'_{m'_\sigma} \tilde{\alpha}'_{m'_\sigma}} \sum_{p_1 \alpha_1; \ldots; p_{n_\sigma} \alpha_{n_\sigma}} \sum_{p'_1 \alpha'_1; \ldots; p'_{n'_\sigma} \alpha'_{n'_\sigma}} V_{\tilde{p}_1}^{\tilde{\alpha}_1} V_{\tilde{p}'_1}^{\tilde{\alpha}'_1 *} \cdots V_{p_1}^{\alpha_1} V_{p'_1}^{\alpha'_1 *} \\
\times a_\sigma^\dagger(\tilde{t}_1^\sigma) a_\sigma(\tilde{t}_1'^\sigma) a_\sigma^\dagger(\tilde{t}_2^\sigma) a_\sigma(\tilde{t}_2'^\sigma) \cdots e^{iH_{\text{bath}}t} e^{-iH_{\text{bath}}t} \cdots a_\sigma^\dagger(t_2^\sigma) a_\sigma(t_2'^\sigma) a_\sigma^\dagger(t_1^\sigma) a_\sigma(t_1'^\sigma) \Big],
\end{aligned} \tag{50}$$

with $\alpha_i \in \{L, R\}$. Since the leads are non-interacting we can evaluate the factor $\operatorname{Tr}_{\text{bath}}[\cdots]$ exactly. Due to Wick's theorem one obtains a product of two determinants $\prod_\sigma \det M_\sigma^{-1}$, with the size of M_σ^{-1} given by the number of operators d_σ on the Keldysh contour ($m_\sigma + n_\sigma$). The matrix elements are given by [20, 25]

$$M_\sigma^{-1}(i,j) = i\Delta(t_{K,i}^\sigma, t_{K,j}'^\sigma), \tag{51}$$

where $t_{K,i}^\sigma$ denotes the position of the ith annihilation operator and $t_{K,j}'^\sigma$ the position of the jth creation operator for spin σ on the unfolded Keldysh contour. The hybridization function Δ is given by

$$\Delta(t_K, t'_K) = \begin{cases} \Delta^<(t'-t) \equiv \Delta_L^<(t'-t) + \Delta_R^<(t'-t) & t_K \geq t'_K, \\ \Delta^>(t'-t) \equiv \Delta_L^>(t'-t) + \Delta_R^>(t'-t) & t_K < t'_K \end{cases}, \tag{52}$$

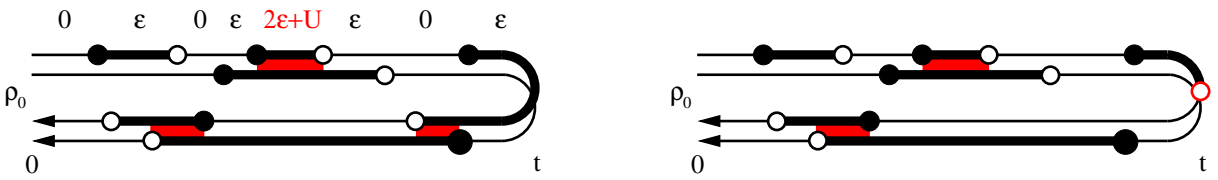

Fig. 2: *Left panel: Segment configuration corresponding to perturbation order 4 for spin up (upper contour) and 2 for spin down (lower contour). Dot creation operators are shown as full circles and annihilation operators as open circles. The segments represent the time intervals in which an electron of the corresponding spin resides on the dot. Right panel: Segment configuration corresponding to the expansion of the current (Eq. (61)) in powers of the dot-lead hybridization. There is a fixed operator d_σ (red open circle) at time t and the hybridization functions connecting to this operator have only a left (L) component. (From Ref. [18])*

with

$$\Delta_\alpha^<(t) = -2i\int_{-\infty}^{\infty}\frac{d\omega}{2\pi}\, e^{-i\omega t}\Gamma^\alpha(\omega)\; f(\omega-\mu_\alpha), \tag{53}$$

$$\Delta_\alpha^>(t) = 2i\int_{-\infty}^{\infty}\frac{d\omega}{2\pi}\, e^{-i\omega t}\Gamma^\alpha(\omega)\big(1-f(\omega-\mu_\alpha)\big). \tag{54}$$

If the bath density of states is flat and centered at zero with a Fermi-function like cutoff at $\omega=\pm\omega_c$,

$$\Gamma^\alpha_{\text{flat}}(\omega) = \frac{\Gamma^\alpha}{\big(1+e^{\nu(\omega-\omega_c)}\big)\big(1+e^{-\nu(\omega+\omega_c)}\big)}, \tag{55}$$

one obtains in the limit $T\ll\omega_c$ the expression [18]

$$\Delta^{</>}_{\text{flat}}(t) \simeq \Gamma\left(\frac{\cos(\frac{V}{2}t)}{\beta\sinh(\frac{\pi}{\beta}t)} - \frac{e^{\pm i\omega_c t}}{\nu\sinh(\frac{\pi}{\nu}t)}\right). \tag{56}$$

To evaluate the trace over the impurity states in Eq. (50), $\mathrm{Tr}_d[\cdots]$, it is useful to employ the segment representation introduced for impurity models with density-density interactions in Ref. [24]. The sequence of dot creation and annihilation operators uniquely determines the occupation of the dot at each time, and we can represent the time evolution using collections of segments for spin up and down electrons as shown in Fig. 2. Each segment depicts a time interval for which an electron with corresponding spin resides on the dot. The trace over the impurity states can then simply be expressed as

$$\mathrm{Tr}_d\left[\cdots\right] = \rho_{\text{imp}}(c)\exp\left[-i\varepsilon_d\sum_\sigma\left(l^\sigma_{\text{forward}}-l^\sigma_{\text{backward}}\right) - iU\left(l^{\text{overlap}}_{\text{forward}}-l^{\text{overlap}}_{\text{backward}}\right)\right]. \tag{57}$$

Here, $\rho_{\text{imp}}(c)$ is the element of the impurity density matrix which is compatible with the operator sequence $c=\{t^\sigma_{K,1},\ldots,t^\sigma_{K,m_\sigma+n_\sigma};t'^\sigma_{K,1},\ldots,t'^\sigma_{K,m'_\sigma+n'_\sigma}\}$ (assumed here to be 1 for configurations which start and end with an empty dot and zero otherwise), l^σ the length of the segments for spin σ and l^{overlap} the length of the overlap between spin up and down segments.

Hence, the Monte Carlo simulation samples collections c of segments on the doubled Keldysh contour (one for each spin) according to their weight

$$w(c) = \prod_\sigma i^{m_\sigma + m'_\sigma} (-i)^{n_\sigma + n'_\sigma} \det M_\sigma^{-1} \, dt^{m_\sigma + m'_\sigma + n_\sigma + n'_\sigma} \, \mathrm{Tr}_d \left[\cdots \right] \tag{58}$$

As in the equilibrium simulations [24], these segment configurations can be sampled using local updates: i) insertion/removal of a segment, ii) insertion/removal of an anti-segment (empty space between segments) and iii) shifts of segment end-points. In order to use fast update formulas similar to those discussed in Sec. 3 one should store and manipulate the matrices M_σ, that is, the inverse of the matrices defined in Eq. (51).

4.2 Measurement of the Green function, density and double occupancy

The Green functions can be obtained from the matrix M in a procedure analogous to the one proposed for imaginary-time simulations in Ref. [24]. Particularly simple is the calculation of the density and double occupancy. From the segment representation it immediately follows that $n_\sigma(t)$ is the probability to have a segment of spin σ present at time t, while $n_\uparrow n_\downarrow(t)$ is the probability to find overlapping segments at time t (taking into account the phases ϕ_c of the Monte Carlo configurations):

$$n_\sigma(t) = \frac{\big\langle \phi_c \, \delta(\text{segment of type } \sigma \text{ at } t) \big\rangle_{|w_c|}}{\langle \phi_c \rangle_{|w_c|}}, \tag{59}$$

$$n_\uparrow n_\downarrow(t) = \frac{\big\langle \phi_c \, \delta(\text{segments of type } \uparrow \text{ and } \downarrow \text{ at } t) \big\rangle_{|w_c|}}{\langle \phi_c \rangle_{|w_c|}}. \tag{60}$$

4.3 Current measurement

The current $I_{L\sigma} = -2 \, \mathrm{Im} \sum_{p \in L} V^L_{p,\sigma} \langle a^{L\dagger}_{p,\sigma} d_\sigma \rangle = -2 \, \mathrm{Im} \left\langle \tilde{a}^\dagger_{L,\sigma} d \right\rangle$ can be measured as explained in Ref. [20]. We expand the quantity

$$I_{L\sigma}(t) = -2 \, \mathrm{Im} \, \mathrm{Tr} \, \rho_0 \Big(\tilde{\mathcal{T}} e^{i \int_0^t ds H_{\mathrm{mix}}(s)} \Big) e^{itH_{\mathrm{loc}}} \, \tilde{a}^\dagger_{L,\sigma} \, d_\sigma \, e^{-itH_{\mathrm{loc}}} \Big(\mathcal{T} e^{-i \int_0^t ds H_{\mathrm{mix}}(s)} \Big) \tag{61}$$

in powers of H_{mix}, which leads to the same collection of diagrams as discussed above, except that there is now an operator d_σ fixed at time t and that the hybridization functions Δ connecting to this operator have only an L-component

$$M^{-1}_\sigma(i,j) = i\Delta_L(t^\sigma_{K,i}, t'^\sigma_{K,j}) + i\Delta_R(t^\sigma_{K,i}, t'^\sigma_{K,j}) \big(1 - \delta_{t, t^\sigma_{K,i}} \big). \tag{62}$$

Having identified the Monte Carlo configurations c (illustrated in the right panel of Fig. 2) and their weights w_c we can implement a random walk based on $|w_c|$ and measure the current as

$$I_{L\sigma} = \sum_c w_c = \langle \phi_c \rangle_{|w_c|} \sum_c |w_c|. \tag{63}$$

In contrast to the density measurement (which was based on an expansion of the identity so that $\sum_c |w_c| = 1/\langle \phi_c \rangle_{|w_c|}$) we cannot directly measure the normalization factor $\sum_c |w_c|$. One

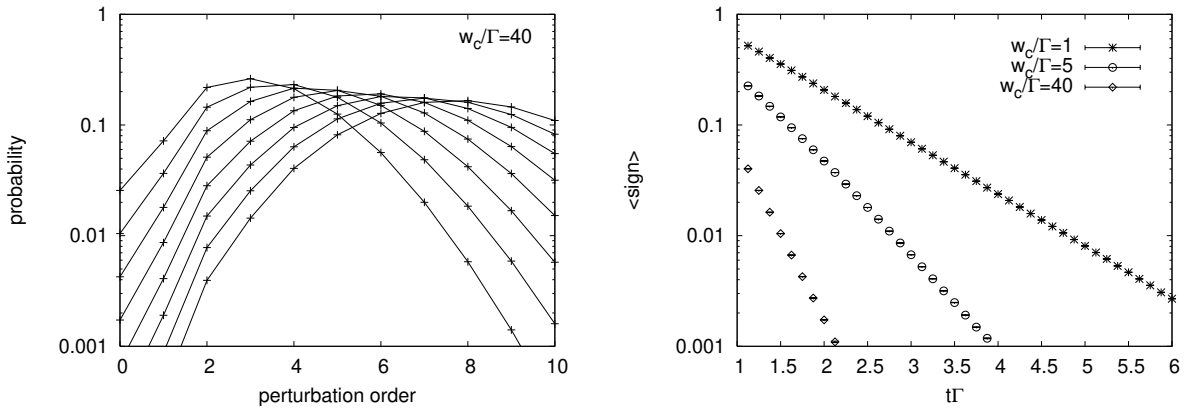

Fig. 3: *Distribution of perturbation orders and average sign obtained using the hybridization expansion algorithm for a non-interacting dot with soft cutoff, $T = 0$, $V = 0$, $\varepsilon_d/\Gamma = -0.5$ and a single fermion species. Left panel: distribution of perturbation orders for different lengths of the contour ($t\Gamma = 1.25, 1.50, \ldots, 3$ from left to right) and cutoff $\omega_c/\Gamma = 40$. The average perturbation order grows $\sim t$. Right panel: average sign as a function of time for the indicated values of the cutoff. (From Ref. [18])*

possibility to get rid of this unknown factor is to consider the ratio $I/I^{(1)}$ between the current and the lowest order contribution $I^{(1)}$ which can be calculated analytically. Since

$$I^{(1)}_{L\sigma} = \big\langle \phi_c \, \delta(c \text{ 1st order}) \big\rangle_{|w_c|} \sum_c |w_c| \tag{64}$$

we can measure the current as

$$I_{L\sigma} = I^{(1)}_{L\sigma} \frac{\big\langle \phi_c \, \big\rangle_{|w_c|}}{\big\langle \phi_c \delta(c \text{ 1st order}) \big\rangle_{|w_c|}}. \tag{65}$$

5 Perturbation order and average sign

If we switch on the interaction (weak-coupling approach) or hybridization (strong-coupling approach) at time $t = 0_+$, the average perturbation order increases approximately linearly with the time interval to be simulated. This results in a dynamical sign problem: the factors of $(\pm i)$ associated with each order of the expansion and the complex determinants mean that the average sign of the diagrams contributing to any quantity decays exponentially as the perturbation order is increased. Figure 3 presents results obtained using the hybridization expansion algorithm on a model of spinless fermions. The same qualitative behavior is found in interacting models and in the weak coupling algorithm. The left panel shows the distribution of perturbation orders for simulations over different time intervals. The mean perturbation order can be estimated from the positions of the maxima in these curves. The right pannel shows the average sign, which decays exponentially with perturbation order or length of the time interval to be simulated.
In practice, accurate measurements of physical quantities can be obtained for $\langle \text{sign} \rangle \gtrsim 0.001$, and whether a steady state can be reached depends on the method, the parameters, and the observable. Non-zero temperature and voltage bias tend to reduce the sign problem, but not

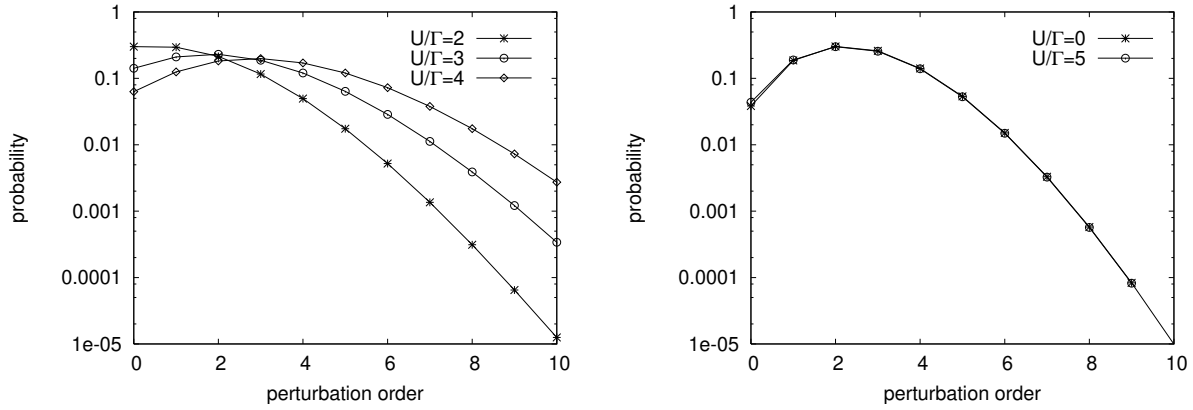

Fig. 4: *Distribution of perturbation orders for different values of the interaction U, for $T = 0$, $V = 0$, ε_d+$U/2 = 0$. The left panel shows the distribution of perturbation orders for the weak-coupling algorithm ($t\Gamma = 1$, infinite bandwidth), where the average perturbation order grows $\sim U$. Right panel: distribution of perturbation orders for the hybridization expansion algorithm ($t\Gamma = 1.5$, $\omega_c/\Gamma = 10$). Here there is almost no dependence on the interaction strength. (From Ref. [18])*

enough to enable simulations on significantly longer contours. The important effect of a non-vanishing voltage bias is to accelerate the relaxation into the steady state, at least in the weak-coupling approach.

The left panel of Fig. 4 shows that in the weak-coupling approach, the average perturbation order (at fixed t) depends on the interaction strength. As in the imaginary-time version of this algorithm [26], the perturbation order grows roughly linearly with increasing U.

In the hybridization expansion algorithm (right panel of Fig. 4), the average perturbation order is essentially independent of interaction strength. This is in contrast to the imaginary-time version of this algorithm [24], where the perturbation order decreases with increasing interaction strength. From Eq. (58) it follows that the interaction term merely adds a phase to the Monte Carlo weight and therefore does not affect $|w(c)|$. While the algorithm can treat strong interactions, it is limited to finite bandwidth, since the average perturbation order diverges as the bandwidth goes to infinity (see cutoff dependence in the right hand panel of Fig. 3).

6 Results: Interaction quench calculations

For practical real-time calculations, the weak-coupling QMC approach turned out to be more useful than the hybridization-expansion QMC method. In particular, this method allowed to obtain accurate current-voltage data for quantum dots (except in the low-voltage regime), and it enabled pioneering nonequilibrium DMFT studies [30–33]. We will illustrate it in this section with interaction quench data for quantum dots, taken from Ref. [19]. Since we consider non-interacting initial states in these simulations, only the real-time branches of the contour need to be considered, and we can use the formalism presented in Sec. 3. Temperature enters only as a parameter in the lead correlators, so that arbitrary temperatures, including $T = 0$, can be treated.

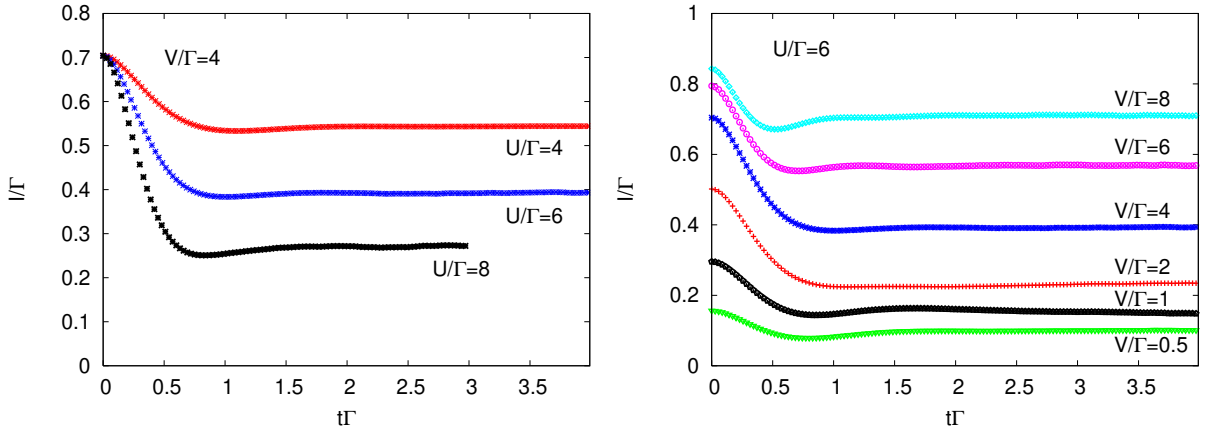

Fig. 5: *Left panel: Time evolution of the current for $V/\Gamma = 4$ and different interaction strengths (bath temperature $T = 0$). In the initial state, the current is given by the steady state current through the non-interacting dot. At time $t = 0_+$, the interaction is turned on. After a time of a few inverse Γ, the current saturates at the value corresponding to the steady state current in the interacting dot. Right panel: Analogous data for different voltage biases and fixed interaction strength $U/\Gamma = 6$. (From Ref. [19])*

6.1 Convergence to the long-time limit: large bias voltage

At time $t = 0$, the system is noninteracting but subject to an applied voltage bias V, so a current $I_0(V)$ corresponding to the noninteracting model is flowing through the dot. At $t = 0_+$ the interaction is turned on and the system relaxes into the steady-state configuration appropriate to the interacting model. The left panel of Fig. 5 shows the time dependence of the current calculated for the large bias voltage $V/\Gamma = 4$ and several interaction strengths. The current initially decreases sharply, overshoots and eventually relaxes back up to the new steady-state value. The interaction-dependence of the steady-state current is a consequence of the Coulomb blockade physics, apparent even at the large voltages studied here.

For intermediate and large voltage bias ($V/\Gamma \gtrsim 2$) and not too large interaction ($U/\Gamma \lesssim 8$) the time required for convergence to the steady state is $t\Gamma \approx 2$, essentially independent of interaction strength. Given the scaling of the perturbation order (and hence the sign problem) with U and t, interactions up to $U/\Gamma \lesssim 10$ are accessible with moderate computational effort.

In the right panel of Fig. 5 we plot the time evolution of the current for fixed $U/\Gamma = 6$ and several voltage biases. For voltages $V/\Gamma \gtrsim 2$, even though the transient behavior is clearly voltage-dependent, the current settles into the new steady state after a time $t\Gamma \approx 2$. However, as the voltage is decreased below $V/\Gamma \approx 2$ the transient time increases. At $V = \Gamma$ the long time limit is attained only for $t\Gamma \gtrsim 3$ and as V is further decreased the approach to the asymptotic behavior becomes even slower.

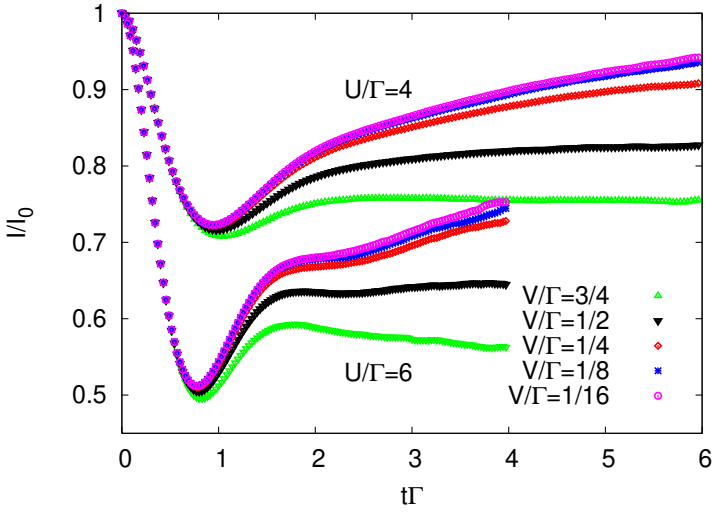

Fig. 6: *Interaction quench in the small-voltage regime ($T = 0$): Ratio of interacting to non-interacting current for $U/\Gamma = 4$ and $U/\Gamma = 6$ and indicated voltage biases. For $V/\Gamma \lesssim 0.5$ the time needed to reach the steady state grows much beyond the largest time accessible in the Monte Carlo simulation. (From Ref. [19])*

6.2 Convergence to the long-time limit: small bias voltage

To better analyze the approach to the steady state at small voltages we present in Fig. 6 the time dependence of the current for several smaller voltages and two interaction strengths. For better comparison, we plot here the ratio I/I_0 of the interacting current I to the noninteracting current I_0. One sees that as V is decreased or U is increased the evolution of the current from the post-quench minimum to the long-time steady state value takes an increasingly long time. Since the longest accessible time is $t\Gamma \approx 6$ for $U/\Gamma = 4$ and $t\Gamma \approx 4$ for $U/\Gamma = 6$, the accurate measurement of I becomes impossible in the small-voltage regime. However the short-time transient behavior is accessible at all voltages. While the ratio $(I/I_0)(t)$ is clearly voltage dependent at higher biases, the data seem to converge as V is reduced to a non-trivial curve with a pronounced minimum near an only weakly U-dependent time $t\Gamma \approx 1$.

It is plausible that the increasingly slow convergence as $V \to 0$ is a signature of the Kondo effect, which is characterized by an energy scale which becomes exponentially small as U increases. After the interaction quench, the Kondo resonance has to be built up as time progresses, and in the limit $V \to 0, T \to 0$ this requires an increasingly large number of interaction vertices and hence an increasingly long simulation time. One expects that the time needed to evolve into the steady state is proportional to the inverse of the associated energy scale.

The slow relaxation becomes an issue in the linear response regime, where the noninteracting and interacting currents are very similar. For $V/\Gamma \gtrsim 0.5$, where the interacting current is substantially smaller than I_0, a useful estimate of I seems possible, even though in the voltage window up to $V/\Gamma \approx 2$ a small drift in the current may remain up to the longest accessible times. This drift makes it difficult to define reliable error bars on I. For $V/\Gamma \lesssim 0.25$, an accurate estimate is not possible from the interaction quench procedure, but the current is very close to the linear response value.

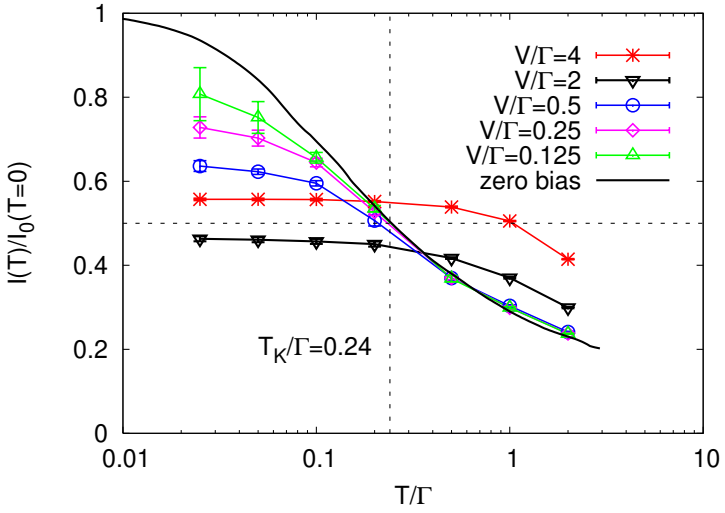

Fig. 7: *Temperature dependence of the ratio of the interacting current at temperature T to the noninteracting current at $T = 0$ for the indicated values of the voltage bias. The interaction strength is $U/\Gamma = 6$. The symbols show Monte Carlo results, the black line the analytical curve for $V \to 0$ extracted from Ref. [34] and plotted for $T_K/\Gamma = 0.24$. (From Ref. [19])*

6.3 Temperature dependence

It is also of interest to examine the temperature dependence of the current. The interplay between voltage and temperature as the Kondo regime is approached presents an interesting problem. One expects that as the temperature is increased, the Kondo effect gets washed out and the simulations would therefore more readily converge even at small bias voltages. The temperature dependence of the current calculated from the interaction quench for $U/\Gamma = 6$ and several values of the voltage bias is plotted in Fig. 7. In the linear response regime ($V/\Gamma = 0.125$, 0.25) the ratio of the interacting current $I(T)$ to the noninteracting current $I_0(T{=}0)$ exhibits a strong temperature dependence, even at $T/V \ll 1$. The temperature dependence arises because lowering the temperature strengthens the Kondo resonance and leads to an increase in the interacting current. The temperature dependence for small voltage bias ($V/\Gamma = 0.125$) approaches the analytical result for the temperature dependent zero-bias conductance in Ref. [34] and thus allows us to estimate (from the temperature at which $I(V{\to}0) = I_0/2$) the Kondo temperature as $T_K/\Gamma \approx 0.24$, in good agreement with the estimate from the formula [35]

$$T_K \approx U\Big(\frac{\Gamma}{2U}\Big)^{1/2} e^{-\pi U/8\Gamma + \pi\Gamma/2U}, \tag{66}$$

which is valid in the strong correlation regime and for $U/\Gamma = 6$ yields $T_K/\Gamma = 0.21$.

As V is increased the temperature dependence is weakened. At intermediate values of V, in the Coulomb blockade regime ($V/\Gamma = 2$), the current has little temperature dependence at low T. At large voltage bias ($V/\Gamma = 4$), correlation effects are significantly weakened due to the voltage, as is evident from the increase in I/I_0. The current in this regime remains insensitive to temperature at low T.

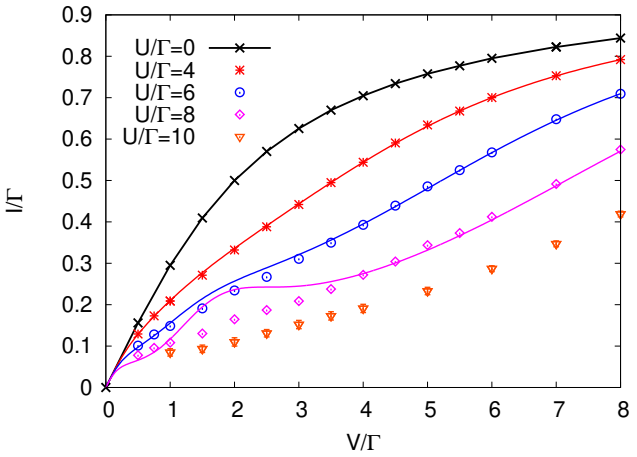

Fig. 8: *Current-voltage characteristics of the single-orbital Anderson impurity model. The symbols show Monte Carlo data for U/Γ=4, 6, 8, 10, while the lines correspond to the fourth order perturbation calculation of Ref. [36]. The Monte Carlo results have been obtained by means of U-quenches at T=0. Error bars are on the order of the symbol size. (From Ref. [19])*

6.4 Current-voltage characteristics

We now apply the weak-coupling QMC approach to compute the current-voltage characteristics of the Anderson impurity model at half-filling.

Figure 8 shows the $T = 0$ result obtained using interaction quenches ($\omega_c/\Gamma = \nu\Gamma = 10$, essentially the wide-band limit). The black curve shows the monotonic increase of the non-interacting current with increasing applied bias voltage. The red, blue and pink lines show the interacting current for $U/\Gamma = 4$, 6, and 8 predicted by fourth order perturbation theory [36]. Consistent with analytical arguments [37, 38], the interacting current initially rises with the same slope as the non-interacting current, and reaches the non-interacting value also in the large-voltage limit. At intermediate values of V, interaction effects suppress the current (Coulomb blockade). In fourth order perturbation theory, a hump appears in the I-V curve around $V/\Gamma = 2$ for $U/\Gamma = 6$ and 8. At even larger U (clearly outside the range of applicability) fourth order perturbation theory will presumably lead to a negative differential conductance at intermediate V. The Monte Carlo data for $U/\Gamma = 4$, 6, 8, and 10 are shown by the red stars, blue circles, pink diamonds, and orange triangles, respectively. Since these are U-quench results for $T = 0$, only $V/\Gamma \gtrsim 0.5$ data are shown. In the large voltage regime ($V/\Gamma \gtrsim 4$), the numerical results agree with the prediction from fourth order perturbation theory. Apparently, the fast decay of the Green functions for large voltage bias simplifies the diagram structure such that fourth order in Σ is sufficient at $V/\Gamma \gtrsim 4$. At intermediate voltages, $1 \lesssim V/\Gamma \lesssim 3$, differences between the Monte Carlo data and fourth order perturbation theory appear. The essentially exact numerical data show no prominent hump feature near $V/\Gamma = 2$, and hence no negative differential conductance in the intermediate to strong correlation regime. The data in Fig. 8 however indicate that fourth order perturbation theory yields correct results over the entire voltage range for $U/\Gamma < 4$. For larger interactions, and in particular around $V/\Gamma \approx 2$ more complicated self energy diagrams become important.

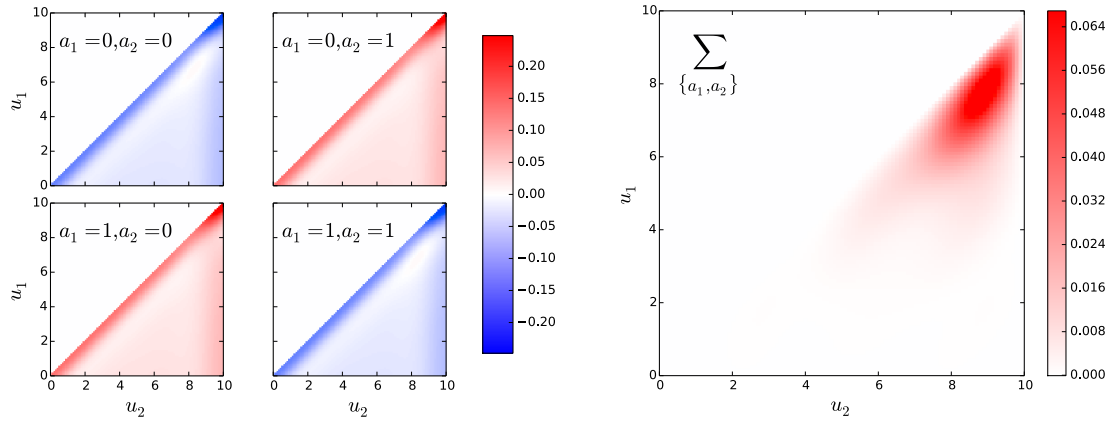

Fig. 9: *Left panels: Color map of the real part of the integrand of Q_2 as a function of the two times u_1 and u_2 (impurity model with $\mu_L = \mu_R = 0$, $T = 0$ and $t = 10$). The four panels correspond to the four possible values of the two Keldysh indices a_1 and a_2. Right panel: Integrand after summation over the Keldysh indices. (From Ref. [39])*

7 Sampling of connected diagrams

The Monte Carlo algorithms described in Sec. 3 and 4 sample both connected and disconnected weak- or strong-coupling diagrams. This is the main reason why the perturbation order grows approximately proportional to the maximum simulation time t and the average sign drops exponentially with t. Since the formulation of these algorithms, alternative QMC approaches have been developed [39, 40], which eliminate the disconnected diagrams. In this section, we briefly discuss the main aspects of these algorithms.

7.1 Weak-coupling approach

Instead of sampling the "partition function" $\tilde{\mathcal{O}} = 1$ (Eq. (12)) and accumulating appropriate estimators for different observables, one can directly implement a weak-coupling diagrammatic expansion for some given observable Q [39],

$$Q(U) = \sum_{n=0}^{\infty} Q_n U^n, \quad Q_n = \sum_{C_n} w_Q(C_n). \tag{67}$$

In this short-hand notation, C_n denotes a configuration of order n and $\sum_{C_n}$ contains the integrations of the vertex positions over the Keldysh contour. The weight $w_Q(C_n)$ includes the $\pm i$ factors from the expansion and a determinant of a matrix whose elements are bath Green functions, analogous to that discussed in Sec. 3.

Instead of parametrizing time on the Keldysh contour by the Keldysh time t_K, one can introduce the pair (t, a), where t is the physical time and the Keldysh index a=0, 1 determines the forward or backward branch of the contour. The important observation in Ref. [39] was that the explicit summation over Keldysh indices eliminates the contribution of the disconnected diagrams from Q_n and allows to absorb significant cancellations between individual diagrams. This leads to a decay of the integrand away from the time t for which the observable is computed, as is

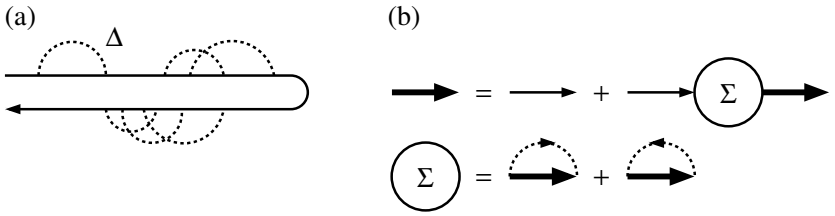

Fig. 10: *Panel (a): Example of a hybridization expansion diagram with a backbone formed by atomic propagators (thin solid lines) and "self-energy" insertions with one, two and three connected hybridization lines (directions left unspecified). Panel (b): NCA pseudo-particle Green function (thick arrow) defined in terms of the atomic propagator (thin arrow) and the NCA self-energy (circle) via the pseudo-particle Dyson equation.*

illustrated in Fig. 9 for the n=2 contribution to the local charge of an impurity model at $t = 10$. The four panels on the left show the real parts of the integrands of Q_2 as a function of the two real-time variables u_1 and u_2 for the indicated combinations of the Keldysh indices a_1 and a_2. The right panel plots the integrand after summation over Keldysh indices. The result is now real and the function is indeed peaked near the measurement time t=10, which suggests that with this approach, large t become more easily accessible. (In quantum dot problems, where the long-time limit is determined entirely by the bath, even $t\to\infty$ can be accessed.)

Implementing a Monte Carlo sampling similar to the one described in Sec. 3 one can measure the ratios Q_n/Q_0 and hence (using an exact evaluation of Q_0) the different terms in the expansion (67). It should be noted though that the summation over the Keldysh indices requires the evaluation of 2^n determinants at order n, so as long as the required orders increase with the measurement time t, the computational effort grows as in a simulation with an exponentially scaling sign problem. At long times, the elimination of the disconnected diagrams should however lead to a slower increase in the relevant orders with t and thus a computational advantage over the method presented in Sec. 3. A downside of the approach is that each observable has to be sampled separately, while the "partition function" sampling allows to measure any observable in one go, including the two-time Green functions which are essential for nonequilibrium DMFT.

7.2 Strong-coupling approach

In the strong-coupling formalism, diagrams with disconnected insertions of hybridization lines (Fig. 10(a)) can be eliminated by defining pseudo-particle propagators for the different atomic states, which resum certain subclasses of diagrams. For example, in the noncrossing approximation (NCA) [41], one sums up all hybridization-expansion diagrams with no crossing hybridization lines by defining a pseudo-particle self-energy as the product of a single hybridization line and a pseudo-particle Green function, and solving a pseudo-particle Dyson equation, in which the bare pseudo-particle propagator is given by the atomic Green function (Fig. 10(b)). At the second oder (one-crossing approximation) [42], one considers pseudo-particle self-energy diagrams with two connected hybridization lines, at third order those with three connected hybridization lines, etc.

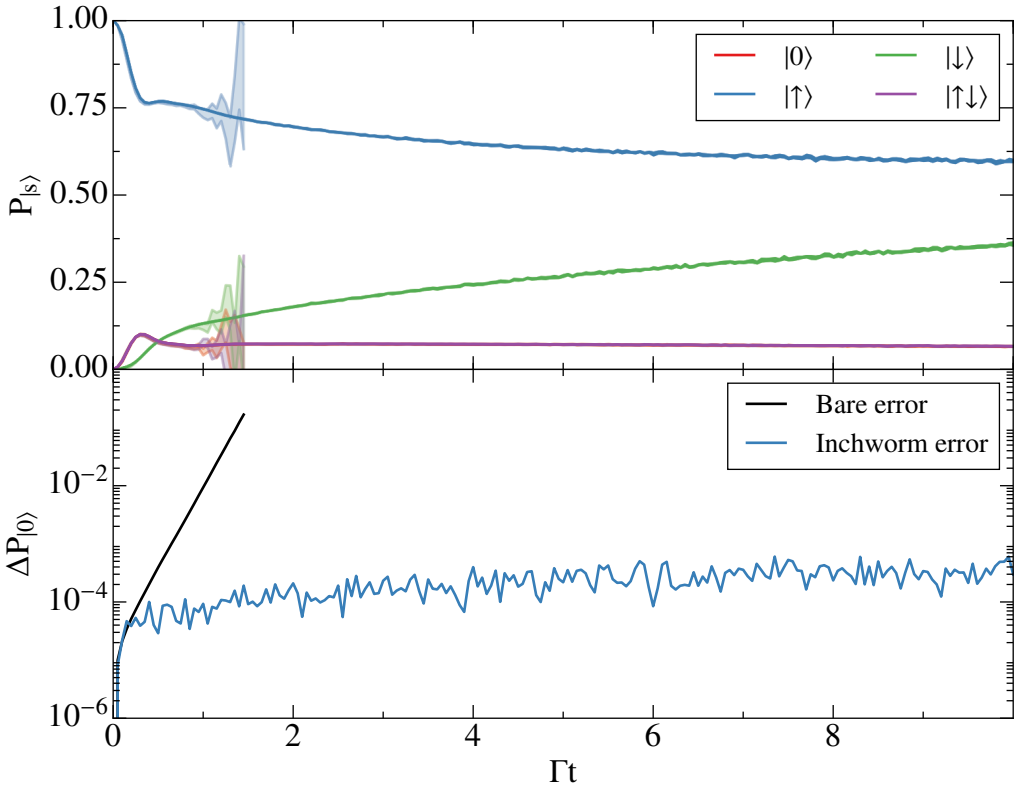

Fig. 11: *Upper panel: Evolution of the local state population for the initial state* $|\uparrow\rangle$ *(*$U = -2\varepsilon = 8\Gamma$ *and* $\beta\Gamma = 50$*). Faint colors show the bare hybridization expansion result for times* $\Gamma t < 1.5$*, while the solid lines plot the inchworm result. Lower panel: Error estimate for the data in the upper panel. (From Ref. [40])*

The implementation of this scheme on the Keldysh contour has been discussed in detail in Ref. [14]. The computational effort for the evaluation of the pseudo-particle self-energy however grows rapidly with increasing order, since each additional hybridization line implies two internal time integrals, each hybridization line has two possible directions (forward or backward) and in a spinful model two spin flavors. Also the number of distinct diagram topologies rapidly increases. Practical calculations have thus been mainly limited to NCA and OCA. A significant step forward occurred with the development of the inchworm approach [40], which uses a Monte Carlo sampling approach to evaluate the internal time integrals. With this method, self-energy diagrams up to fourth or even higher orders can be evaluated.

Thanks to the elimination of disconnected diagrams, longer maximum times t than in the standard hybridization expansion of Sec. 4 can be accessed. This is relevant for example in situations where a slow initial relaxation hampers the measurement of a steady state property. Figure 11 shows the evolution of the probabilities for the four different impurity states after the sudden switch-on of the coupling to the bath at time $t = 0_+$, for a system which is initially in the state $|\uparrow\rangle$. In contrast to the conventional bare hybridization expansion (faint colors), which only allows to calculate the dynamics up to $t\Gamma \approx 1$, the inchworm simulation can track the relaxation almost to the steady state, which has equal probabilities for the states $|\uparrow\rangle$ and $|\downarrow\rangle$.

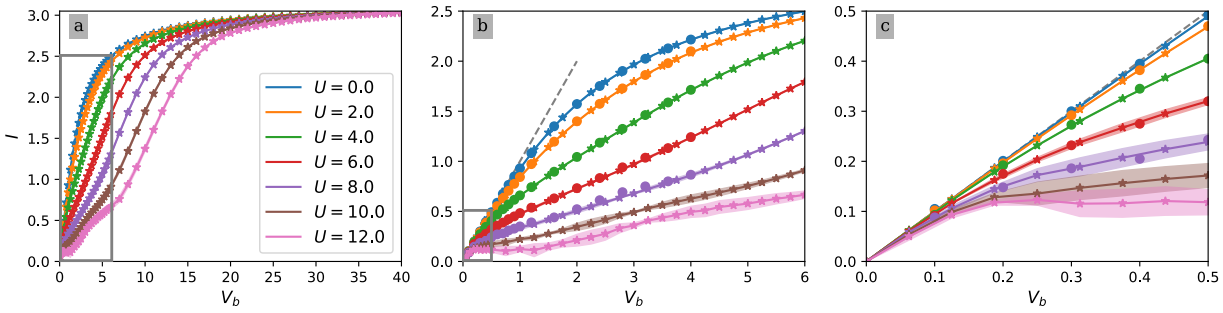

Fig. 12: *Current-voltage characteristic $I(V_b)$ of the Anderson impurity model. Panel (a) shows the full voltage range and panels (b,c) the intermediate and low-V_b behavior. The stars show the results obtained by TCI, while the circles are benchmark data calculated with QMC [45]. (From Ref. [46])*

8 Beyond Monte Carlo

8.1 Tensor cross interpolation

A recent innovation, which may eliminate the need for Monte Carlo sampling in situations which can be handled with perturbation orders $\lesssim 30$, is the tensor cross interpolation (TCI) of multivariable functions [43, 44]. In our case, the multivariable functions of interest are the diagram weights, which depend on a certain number of Keldysh time variables. On a discretized time grid, an n-dimensional function $f(t_{K,1}, t_{K,2}, \ldots, t_{K,n})$ becomes an n-way tensor, which can be factorized by TCI into a tensor train (or matrix-product state),

$$f(t_{K,1}, t_{K,2}, \ldots, t_{K,n}) \approx T_1(t_{K,1}) \cdot T_2(t_{K,2}) \cdot \ldots \cdot T_n(t_{K,n}). \tag{68}$$

where the T_i are matrices whose dimension depends on the properties of the function f and the desired accuracy of the interpolation. The important point is that this factorization reduces an n-dimensional integral to products of one-dimensional integrals, which can be efficiently computed if the matrix dimensions are sufficiently low [44].

Recent studies have applied the TCI approach to both the weak-coupling and strong-coupling diagrammatic schemes discussed in Sec. 7 and obtained promising results.

8.2 Weak-coupling expansion with TCI

The general idea of evaluating Feynman diagrams with the help of TCI has been introduced in Ref. [44], which also demonstrated some applications to real-time impurity problems within the general framework described in Sec. 7.1. Highly accurate results with perturbation orders up to ≈ 25 have recently been published in Ref. [46]. As an illustration, Fig. 12 shows the current-voltage characteristics of the Anderson impurity model, and demonstrates the approach to the linear-response behavior in the numerically challenging low-V regime, even for strong interactions.

8.3 Strong-coupling expansion with TCI

The evaluation of the self-consistently resummed hybridization expansion diagrams (Sec. 7.2) with the help of TCI is a promising strategy, since this expansion converges rapidly with the diagram order in the strongly-correlated regime [14]. Two related but at the technical level distinct implementations for nonequilibrium steady-state problems have recently been presented in Refs. [47] and [48]. One of them uses a standard TCI decomposition of the hybridization part of the pseudo-particle self-energy integrand [47], and the other a so-called quantics-TCI decomposition [49] of the full pseudo-particle self-energy integrand. In the quantics approach [48], the time variables are expressed in a binary representation, and separate tensors are associated with each bit. Pushing these methods to sufficiently high orders and assessing their efficiency is the subject of ongoing research, but the strong-coupling TCI approach is likely to replace QMC approaches for strongly correlated nonequilibrium impurity problems.

9 Conclusions

The basic idea of the QMC approach for nonequilibrium systems is to evaluate a diagrammatic expansion on the two-leg Keldysh or three-leg Kadanoff-Baym contour using Monte Carlo sampling. We detailed the original weak-coupling and strong-coupling formulations of this approach, which are direct generalizations of the widely used continuous-time QMC methods [17] from the Matsubara axis to two-leg or three-leg contours. We discussed these methods for quantum dot problems, where the bath is given and the main goal is the calculation of some steady-state property (typically the current through the dot). The same machinery can however also be used within nonequilibrium DMFT, where the bath Green functions or hybridization functions are self-consistently computed in the DMFT loop [4]. In this context, the main challenge becomes the calculation of the impurity Green function $G(t, t')$.

Especially the weak-coupling approach has allowed to obtain useful results, both for the current-voltage characteristics of quantum dots [19], and for quenched or electric field driven Hubbard models [4]. In the DMFT context, this method has enabled pioneering studies on dynamical phase transitions [30] and dynamical band flipping [31], which even after more than a decade remain exceptional examples of numerically exact nonequilibrium DMFT results. However, in contrast to equilibrium, where the continuous-time QMC approach is powerful enough for a wide range of typical applications, the real-time incarnation of this method is limited by a dynamical sign problem. Since the average perturbation order grows approximately linearly with the maximum time t, the time evolution is complex, and each operator comes with a prefactor $\pm i$, the average sign in the Monte Carlo sampling drops exponentially with increasing t. This limits the simulations to short times.

A promising strategy to tame the sign problem is to suppress disconnected diagrams, which contribute significantly to the sign cancellations, but not to the measured observables. In the weak-coupling approach, this can be achieved by summing all diagrams with the same real-time positions of operators, but different Keldysh indices [39]. While this summation also comes at

an exponential cost, the available results suggest that the suppression of phase cancellations more than compensates this cost. In the strong-coupling approach, one can switch to a pseudo-particle formalism, and work with propagators which resum all the disconnected hybridization-expansion diagrams with self-energy insertions up to a given order. The inchworm algorithm [40] stochastically evaluates the pseudo-particle self-energies within this formalism.

The most recent development is the explicit evaluation of the integrals over diagram weights via TCI [44]. This approach avoids Monte Carlo sampling and looks promising in situations where the required perturbation order is $\lesssim 30$. The basic idea is to factorize the diagram weights into a tensor-train form. Since this factorization reduces the evaluation of a high-dimensional integral to the numerically much more simple evaluation of products of one-dimensional integrals, it allows to treat high-dimensional functions which would be too expensive to integrate with standard quadrature rules. Different flavors of TCI based impurity solvers are currently being developed and tested and they are likely to outperform the real-time QMC solvers in most applications.

References

[1] A. Georges, G. Kotliar, W. Krauth, and M.J. Rozenberg, Rev. Mod. Phys. **68**, 13 (1996)

[2] D. Goldhaber-Gordon, H. Shtrikman, D. Mahalu, D. Abusch-Magder, U. Meirav and M.A. Kastner, Nature **391**, 156 (1998)

[3] C. Giannetti, M. Capone, D. Fausti, M. Fabrizio, F. Parmigiani, and D. Mihailovic, Adv. Phys. **65**, 58 (2016)

[4] H. Aoki, N. Tsuji, M. Eckstein, M. Kollar, T. Oka, and P. Werner, Rev. Mod. Phys. **86**, 779 (2014)

[5] J. Li and M. Eckstein, Phys. Rev. B **103**, 045133 (2021)

[6] L. Kadanoff and G. Baym, *Quantum Statistical Mechanics* (Benjamin, New York, 1962)

[7] L.V. Keldysh, Zh. Eksp. Teor. Fix. **47**, 1515 (1964) [Sov. Phys. JETP **20**, 1018 (1965)]

[8] F.B. Anders and A. Schiller, Phys. Rev. **B** 74, 245113 (2006)

[9] N. Makri, J. Chem. Phys. **111**, 6164 (1999)

[10] S. Weiss, J. Eckel, M. Thorwart, and R. Egger, Phys. Rev. B **77**, 195316 (2008)

[11] J. Thoenniss, M. Sonner, A. Lerose, and D.A. Abanin, Phys. Rev. B **107**, L201115 (2023)

[12] M. Nayak, J. Thoenniss, M. Sonner, D.A. Abanin, P. Werner, arXiv:2503.02848 (2025)

[13] A. Goker, B.A. Friedman, and P. Nordlander, J. Phys.: Condens. Matter **19**, 376206 (2007)

[14] M. Eckstein and P. Werner, Phys. Rev. B **82**, 115115 (2010)

[15] K.A. Al-Hassanieh, A.E. Feiguin, J.A. Riera, C.A. Busser and E. Dagotto, Phys. Rev. B **73**, 195304 (2006)

[16] S. Kirino, T. Fujii, J. Zhao and K. Ueda, J. Phys. Soc. Jpn. **77**, 084704 (2008)

[17] E. Gull, A.J. Millis, A.I. Lichtenstein, A.N. Rubtsov, M. Troyer, and P. Werner, Rev. Mod. Phys. **83**, 349 (2011)

[18] P. Werner, T. Oka, and A.J. Millis, Phys. Rev. B **79**, 035320 (2009)

[19] P. Werner, T. Oka, M. Eckstein and A.J. Millis, Phys. Rev. B **81**, 035108 (2010)

[20] L. Mühlbacher and E. Rabani, Phys. Rev. Lett. **100**, 176403 (2008)

[21] T. Schmidt, P. Werner, L. Mühlbacher, and A. Komnik, Phys. Rev. B **78**, 235110 (2008)

[22] M. Schiro and M. Fabrizio, Phys. Rev. B **79**, 153302 (2009)

[23] A.N. Rubtsov, V.V. Savkin and A.I. Lichtenstein, Phys. Rev. B **72**, 035122 (2005)

[24] P. Werner, A. Comanac, L. de' Medici, M. Troyer and A.J. Millis, Phys. Rev. Lett. **97**, 076405 (2006)

[25] P. Werner and A.J. Millis, Phys. Rev. B **74**, 155107 (2006)

[26] E. Gull, P. Werner, O. Parcollet, and M. Troyer, Europhys. Lett. **82**, 57003 (2008)

[27] S.M.A. Rombouts, K. Heyde, and N. Jachowicz, Phys. Rev. Lett. **82**, 4155 (1999)

[28] J. Rammer and H. Smith, Rev. Mod. Phys. **58**, 323 (1986)

[29] K. Mikelsons, A. Macridin, and M. Jarrell, Phys. Rev. E **79**, 057701 (2009)

[30] M. Eckstein, M. Kollar, and P. Werner, Phys. Rev. Lett. **103**, 056403 (2009)

[31] N. Tsuji, T. Oka, P. Werner and Hideo Aoki, Phys. Rev. Lett. **106**, 236401 (2011)

[32] M. Eckstein and P. Werner, Phys. Rev. Lett. **107**, 186406 (2011)

[33] E. Canovi, P. Werner and M. Eckstein, Phys. Rev. Lett. **113**, 265702 (2014)

[34] R.M. Konik, H. Saleur, and A.W.W. Ludwig, Phys. Rev. Lett. **87**, 236801 (2001)

[35] A.C. Hewson, *The Kondo Problem to Heavy Fermions*, (Cambridge Univ. Press, 1993)

[36] T. Fujii and K. Ueda, Phys. Rev. B **68**, 155310 (2003)

[37] T.K. Ng and P.A. Lee, Phys. Rev. Lett. **61** 1768, (1988)

[38] L.I. Glazman and M.E. Raikh, Zh. Eksp. Teor. Fiz. **47**, 378 (1988) [JETP Lett. **47**, 452]

[39] R.E.V. Profumo, C. Groth, L. Messio, O. Parcollet, and X. Waintal, Phys. Rev. B **91**, 245154 (2015)

[40] G. Cohen, E. Gull, D.R. Reichman, and A.J. Millis, Phys. Rev. Lett. **115**, 266802 (2015)

[41] H. Keiter and J.C. Kimball, J. Appl. Phys. **42**, 1460 (1971)

[42] T. Pruschke and N. Grewe, Z. Phys. B **74**, 439 (1989)

[43] I. Oseledets and E. Tyrtyshnikov, Linear Algebra and its Applications **432**, 70 (2010)

[44] Y. Nunez Fernandez, M. Jeannin, P.T. Dumitrescu, T. Kloss, J. Kaye, O. Parcollet and X. Waintal, Phys. Rev. X **12**, 041018 (2022)

[45] C. Bertrand, S. Florens, O. Parcollet, and X. Waintal, Phys. Rev. X **9**, 041008 (2019)

[46] M. Jeannin, Y. Nunez-Fernandez, T. Kloss, O. Parcollet, and X. Waintal, arXiv:2502.16306 (2025)

[47] M. Eckstein, arXiv:2410.19707 (2024)

[48] A. Kim and P. Werner, Phys. Rev. B **111**, 125120 (2025)

[49] M.K. Ritter, Y. Nunez Fernandez, M. Wallerberger, J. von Delft, H. Shinaoka, and X. Waintal, Phys. Rev. Lett. **132**, 056501 (2024)